PAPER

Check for updates

Nonlinear generation control with torus metasurfaces

Lei Kang, ID * Charles F. Nelatury ID and Douglas H. Werner ID *

Supporting induced toroidal moments, nanostructures with toroidal topology offer an alternative mechanism for light–matter interaction. Toroidal resonances observed in artificial meta-atoms unambiguously exhibit distinct characteristics originating from their electric and magnetic multipoles. Despite the various nanostructures introduced for toroidal moment excitation, meta-atoms comprising dielectric torus structure, an architecture which naturally provides the topology for toroidal dipole (TD) moments, remain unexplored. On the other hand, the dark-mode nature of resonances in torus metasurfaces enables strong field enhancement and hence the potential for nonlinear optics. Here, third harmonic generation (THG) from planar silicon torus metasurfaces, which support high quality (Q)-factor resonances associated with the bound states in the continuum (BICs) at near-infrared wavelengths, are numerically demonstrated. The properties of the THG signal originating from the electric dipole (ED), TD, magnetic quadrupole (MQ), and magnetic dipole (MD) resonances can be engineered by exploiting the symmetry of the torus nanostructure. A pair of strong chiral resonance modes are observed in the asymmetric resonators with broken in-plane mirror symmetry, enabling elliptically polarized THG signals from the torus metasurfaces under linearly polarized excitations. Dielectric torus metasurfaces supporting quasi-BIC resonances can serve as a powerful platform for light control in both the linear and nonlinear regimes.

1. Introduction

Exploration and exploitation of various multipole moments in light–matter interaction is the foundation of nanophotonics. Characterized by light-induced charge separation and loop currents respectively, electric dipoles (EDs) and magnetic dipoles (MDs) are key to numerous optical phenomena, from fascinating colors in colloidal metal nanoparticles,[1,2] artificial optical magnetism,[3] negative refraction,[4] strong chirality,[5] to anomalous reflection and refraction[6] and the photonic spin Hall effect,[7] to name a few. In stark contrast to EDs and MDs, toroidal moments, which have been studied in a variety of fields[8–11] since their first discussion,[12] are less explored in electromagnetics mainly due to the difficulties in exciting strong toroidal modes. Despite the recent theoretical studies on toroidal electrodynamics,[13–17] toroidal multipoles are not included in the current Mie theory description of the scattering behavior of objects with sizes comparable to the wavelength of light. On the other hand, toroidal moments have been discussed for a series of exotic electromagnetic effects, such as reciprocity and optical activity when combined with magneto-optical, non-linear, or time-varying materials.[18,19]

Department of Electrical Engineering and Center for Nanoscale Science, The Pennsylvania State University, University Park, PA 16802, USA. E-mail: lzk12@psu.edu, dhw@psu.edu

Meta-atoms, *i.e.*, the building blocks of metamaterials, can tailor light–matter interaction on subwavelength scales through structural engineering, offering unprecedent flexibility in producing multipole moments *via* engineering current oscillations. Two recent review articles have provided a comprehensive summary of the development of toroidal metamaterials and metasurfaces.[20,21] The excitation of electromagnetic moments is essentially determined by the symmetry and topology of resonators. A toroidal dipole (TD) is equivalent to currents flowing on the surface of a torus. Based on this understanding, elaborately arranged split ring resonators (SRRs)[22–26] and similar metallic structures[27] forming meta-molecules have demonstrated TDs at microwave and terahertz frequencies. Recently, using an array of asymmetric double-bars obtained from nanofabrication, Dong and coworkers have demonstrated the TD response in the near-infrared region.[28] In these studies, the excitation of TDs can be attributed to (i) phase retardance between individual SRRs in each unit cell[23,27] and (ii) asymmetry of the meta-molecules.[22,24–26,28] On the other hand, the reported TDs can be categorized into two groups, *i.e.*, TD perpendicular to the wavevector ($T \perp k$) and TD parallel to the wavevector ($T \parallel k$), while the latter has potential for high quality (Q)-factor spectra due to its "dark mode" nature.[29,30]

Toroidal moments have also been identified in isolated[31–34] and arrayed dielectric resonators.[35,36] Besides the unique field

confinement configuration in the linear regime due to their topology, TDs have been used to facilitate enhanced nonlinearities in dielectric nanostructures.[31,32,37] Distinct from metallic resonators, electromagnetic response from dielectric structures is simultaneously determined by their geometry and refractive index,[38] enabling light manipulation with extremely low loss.[39,40] Importantly, an analysis based on multipole decomposition[35] has shown that toroidal moments can be identified in dielectric nanostructures under optical excitations. Efforts have recently been made to develop dielectric metasurfaces that exhibit resonances associated with bound states in the continuum (BICs). Corresponding to the localized states that coexist with a continuous spectrum of radiating waves, BICs usually manifest strong energy confinements, infinite Q-factors, and extreme field enhancements. Accordingly, with broken symmetry, the systems supporting quasi-BICs with finite Q-factors have been reported to realize enhanced nonlinearities.[41-46] TD moments associated with BICs have also been observed. He and coauthors have reported the observation of quasi-BIC TD resonances in an array of silicon nanodisk dimers.[47] More recently, You and coauthors have demonstrated that electromagnetically induced transparency (EIT) originates from the coupling between a magnetic TD and two quasi-BICs within a silicon metasurface with off-center air holes.[48] The high-Q nature of TD-BICs represents a new pathway to generating strong toroidal moments in dielectric metasurfaces with a concomitant field enhancement effect. Consequently, a torus metasurface featuring quasi-BIC resonances and toroidal topology represents a promising platform for efficient nonlinear generation with tunable properties. Nevertheless, studies on dielectric torus resonators, which can be considered as the most intuitive structure to support TD resonances, remain rare.

Three-dimensional (3D)[5,49-53] and 2D meta-atoms[54-56] that are non-superimposable on their mirror image have been used to achieve strong chiroptical response, enabling unprecedented flexibility in manipulating the polarization of light. More recently, chiral quasi-BIC resonances[57-59] and enhanced chiral nonlinearities[60-62] have been observed in planar dielectric nanostructures. On the other hand, based on the combinations of electric and magnetic moments with toroidal moments, Papasimakis et al., have demonstrated optical activity in an array of chiral toroidal coils at microwave frequencies.[19] More recently, Kang et al., have reported toroidal circular dichroism (CD) in a bilayer metasurface exhibiting a toroidal dipole moment at frequencies around 15 GHz.[63] However, the role that toroidal topology plays in the observed chiral response is elusive. Dielectric metasurfaces with a toroidal topology capable of supporting chiral quasi-BIC resonances originating from toroidal moments hold great potential as a superior platform for chiral optics.

In this work, we numerically demonstrate that silicon torus metasurfaces can support TD and a series of resonances associated with BICs at near-infrared wavelengths. Optical anisotropy based on nanogrooves enables TD excitation in the torus resonators under illumination of linearly polarized light at normal incidence, giving rise to significantly enhanced third harmonic generation (THG) from the metasurface. More importantly, with broken in-plane mirror (2D-chiral) symmetry, silicon torus resonators having asymmetrically arranged nanogrooves exhibit two sharp chiral resonances associated with an electric dipole (ED), a toroidal dipole, and a magnetic quadrupole (MQ), resulting in a pronounced transmission CD and spin-selective field enhancement effect. Furthermore, our nonlinear simulations show that, under linearly polarized excitations, these two chiral resonances lead to elliptically polarized TH emission in both reflection and transmission. Importantly, the diffraction efficiency and polarization state of the observed THG signals are heavily dependent on the symmetry property of the torus meta-atoms. Our results demonstrate the potential of the torus metasurfaces for light control in both the linear and nonlinear regimes based on their unique topological characteristics.

2. Results and discussion

A unit cell of the silicon (refractive index $n_{Si} = 3.48$) torus metasurface located on top of a glass substrate ($n_g = 1.46$) is illustrated in Fig. 1(a). The nanogrooves introduced on one side ($x > 0$) of the torus resonator not only result in optical anisotropy but also open a leaky channel for quasi-BIC.[64] In fact, the resonance modes observed in Fig. 1 become true BIC when there is no nanogroove. To verify this, through eigenmode simulations, we study a torus structure without nanogrooves in reciprocal space (Fig. S1). The observed Q-factors corresponding to all four modes show a clear divergence behavior, indicating a symmetry-protected BIC associated with each resonance.[65-67] Note that, with a separation angle $\theta = 25°$, the nanogrooves are arranged symmetrically relative to the x-axis (see the inset of Fig. 1(b)). The quasi-BIC properties of the four lowest-frequency modes supported by the structure are studied through COMSOL eigenmode simulations. Since a periodic boundary condition is applied in the x- and y-direction without lateral phase delay, our eigenmode simulations examine the intrinsic response of the metasurface under normal incidence. The eigen-wavelength and Q-factor as a function of the number of nanogrooves (N) and the depth of the nanogrooves (h) are summarized in Fig. 2(b)–(e). One can see that the resonance wavelengths of all four modes are insensitive to N and h, suggesting the robustness of the torus metasurface. On the other hand, the increasing Q-factors with decreasing N and h reveal the quasi-BIC characteristics of the structure. Q-factors slightly increase for the MQ-X and ED + TD modes as N is increased past 4, which could be attributed to the decreased radiation loss of the system. As illustrated in Fig. 1(e), when $N = 7$ and $h = 30$ nm a Q-factor larger than 10^4 is achieved for both modes around 1100 nm wavelength (denoted by the blue and red circles in Fig. 1(d)). To better understand the nature of all four modes, Fig. 1(f–i) shows the corresponding mode profiles. Remarkably, the rotating vectors of magnetic field identified in Fig. 1(f) unambiguously indicate a TD resonance at 1107 nm wavelength, with a concomitant maximum
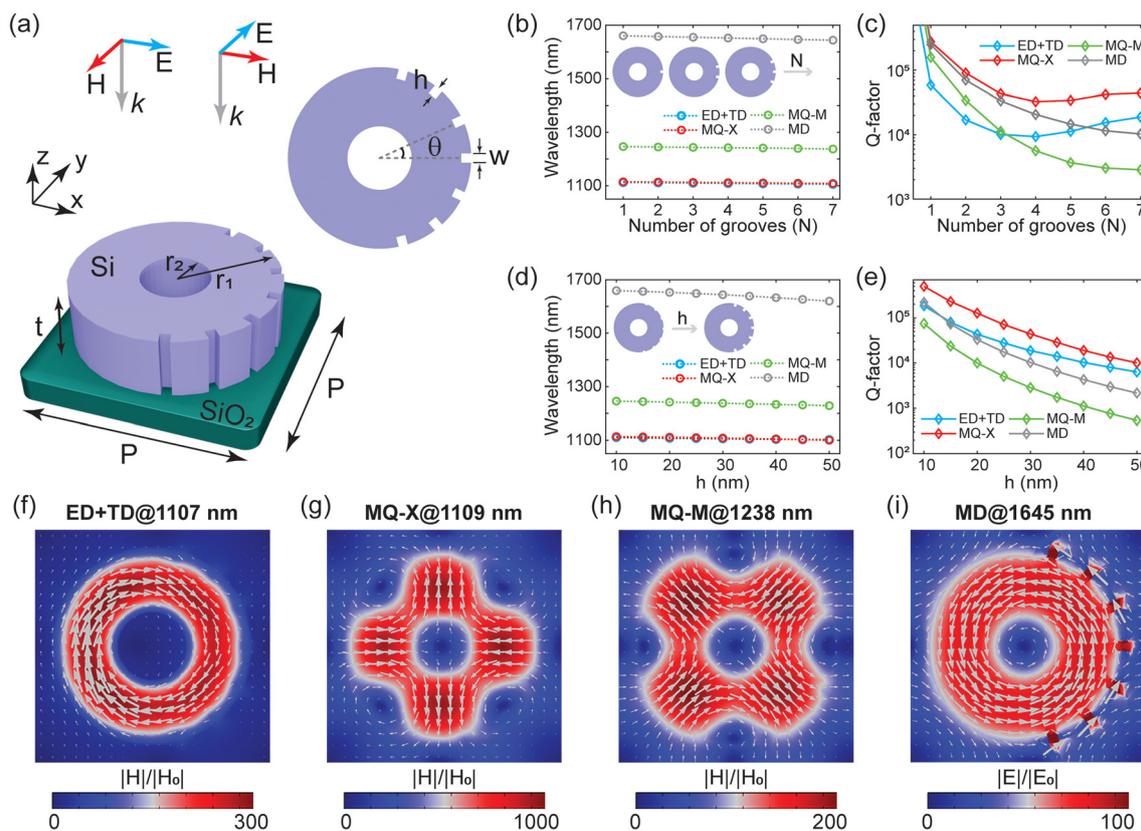
Fig. 1 Torus metasurfaces supporting quasi-BIC resonances. (a) Schematic of a unit cell of the Si torus metasurface. Inset: top view showing the arrangement of the nanogrooves. Geometrical parameters: $P = 700$ nm, $r_1 = 300$ nm, $r_2 = 100$ nm, $t = 220$ nm, $w = 30$ nm, and $\theta = 25°$. The dependences of (b) resonance wavelengths and (c) Q-factors of the four lowest-frequency modes on the number of nanogrooves (N). For results shown in (b) and (c), the depth of nanogrooves h was fixed to 30 nm. The dependences of (d) resonance wavelengths and (e) Q-factors on h. For results shown in (d) and (e), N was fixed to 7. The magnetic field distributions along with the magnetic field vectors cut at the middle of the torus resonator at a (f) TD mode, (g) MQ-X mode, and (h) MQ-M mode. Note the TD mode in (f) is accompanied by an ED mode (see multipolar decomposition results in Fig. 2). (i) The electric field distribution along with the electric field vectors at a MD mode. For results shown in (f)–(i), $N = 7$ and $h = 30$ nm. The magnetic and electric field magnitudes are normalized to those of the incident field, respectively.

field enhancement factor of 300. As seen in the later nonlinear analysis, this observed strongly confined TD resonance gives rise to the enhanced THG signals with properties controlled by the torus structure's symmetry. Furthermore, Fig. 1(g) and (h) show two MQ resonances. Exhibiting the highest Q-factor among the four considered modes, the MQ-X resonance at 1109 nm reveals a maximum field enhancement factor of 1000. We emphasize that, as seen in later discussions, the unique topologies of the TD and the MQ-X modes imply their distinct excitation mechanisms. Moreover, the rotating vectors of electric field seen in Fig. 1(i) mark a MD resonance at 1645 nm wavelength. In contrast to the field confinement effect seen in Fig. 1(f)–(h), at the MD mode the field also concentrates in the nanogrooves, causing the relatively low Q-factor and moderate field enhancement effect. These observed field concentration phenomena in the linear regime reveal the potential of the torus metasurfaces to support enhanced nonlinearities.

As discussed above, the nanogroove-induced anisotropy gives rise to the resonance modes seen in Fig. 1. To further clarify the mode excitation mechanisms, in Fig. 2(a–d) we

show the simulated transmittance spectra of the metasurface ($N = 7$ and $h = 30$ nm) illuminated by x- and y-polarized light at normal incidence. Fig. 2(a) shows that, under x-polarized excitation, the metasurface exhibits a sharp transmission dip around 1106 nm wavelength. Importantly, for x-polarized excitation, only the magnetic field of the incident wave can 'see' the anisotropy. Originating from magnetic Mie resonances, magnetic field oscillations in the $x > 0$ and $x < 0$ regions of the torus become out-of-phase in the resonator, resulting in a rotating magnetic field associated with a TD moment (Fig. 1(f)). Furthermore, Fig. 2(b) indicates that the MQ-X mode seen in Fig. 1(g) can be excited by a y-polarized wave, while the sharp spectrum suggests this mode as a viable candidate for efficient nonlinear generation. The transmittance spectra corresponding to the MQ-M and MD resonances in the torus metasurface are shown in Fig. 2(c) and (d). These behaviors reveal the flexibility in selectively exciting distinct resonances, especially those associated with TD and the MQ-X modes, which are close together in the spectrum, in the torus metasurface based on their polarization sensitivity. To better
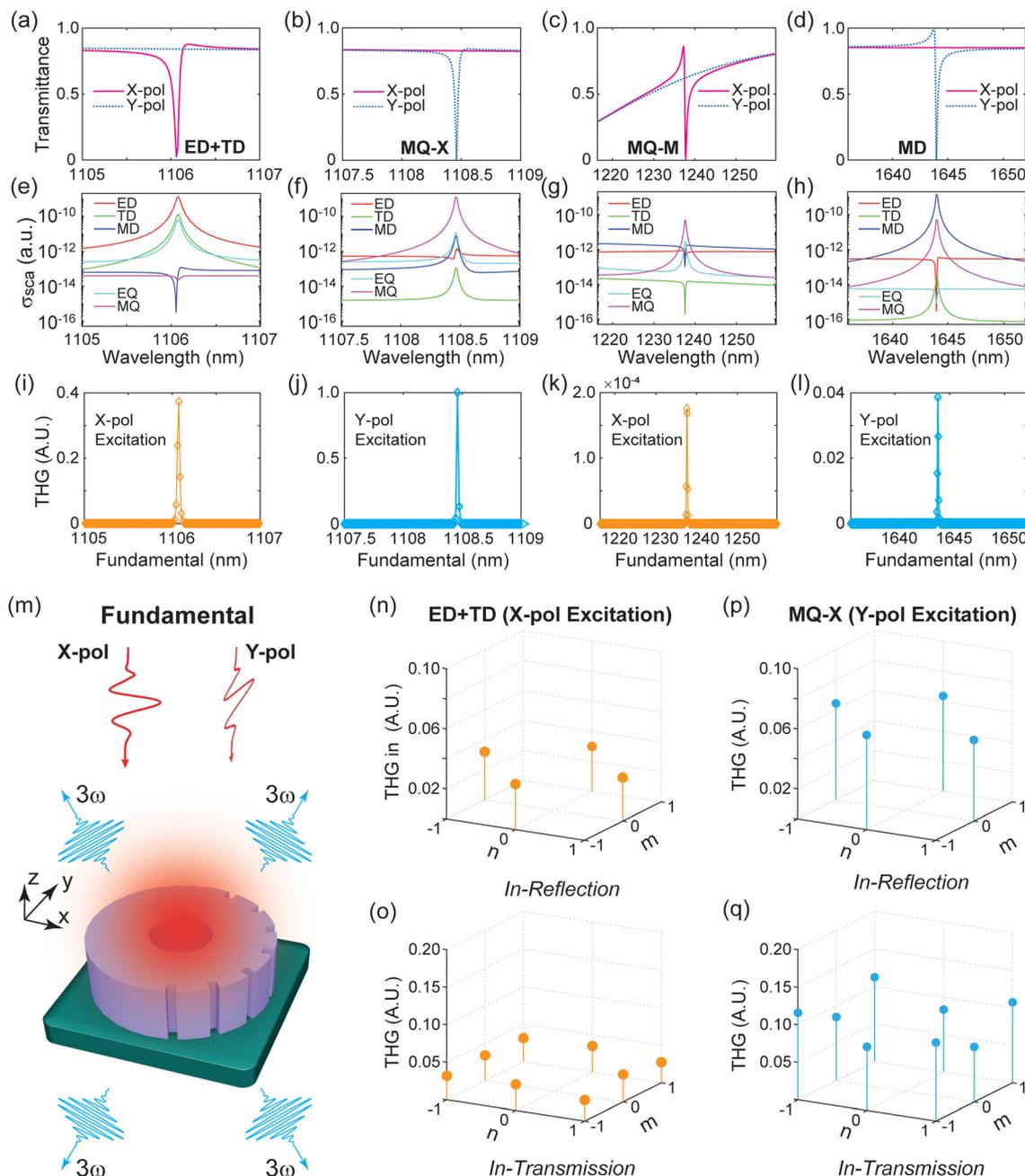
Fig. 2 Enhanced THG in the torus metasurface. (a)–(d) Simulated transmittance spectra ($N = 7$ and $h = 30$ nm). (e)–(h) Multipolar decomposition of scattering cross-sections in terms of electric dipole (ED), toroidal dipole (TD), magnetic dipole (MD), electric quadrupole (EQ), and magnetic quadrupole (MQ). (i)–(l) Simulated spectra of the total THG signal generated from the metasurface. (m) Schematic of the THG diffraction upon x- and y-polarized excitations. TD mode on-resonance THG power distribution between the diffraction orders in (n) reflection and (o) transmission. MQ-X mode on-resonance THG power distribution between the diffraction orders in (p) reflection and (q) transmission.

elucidate the nature of the observed resonances, we perform a multipole decomposition analysis[23] and summarize the results in Fig. 2(e–h). We note that, although the resonance around 1106 nm is ED dominant, a significant contribution from a TD moment is unambiguously identified (Fig. 1(e)). The multipolar contributions observed in Fig. 2(e–h) are consistent with the mode profile analysis summarized in Fig. 1(f–i). We note that the multipole expansion is derived from writing the

Green's function, $G(\mathbf{r}, \mathbf{r}')$ of the inhomogenous wave equation as $\sum_{l,m} g_l(r, r') Y_{lm}^*(\theta', \varphi') Y_{lm}(\theta, \varphi)$. Because the azimuthal symmetry of our system is only slightly broken, an alternative representation which could be applicable in our analysis is the Lommel expansion, which has the form $\frac{e^{-ikR'}}{R'} = \frac{e^{-ikR}}{R} - ik \sum_{m=1}^{\infty} \frac{(k^2 \rho a)^m}{m!} \frac{h_m^{(2)}(kR)}{(kR)^m} \cos^m(\varphi - \varphi')$, where, for cylindri-

cal field coordinates ρ, φ, z, one defines $R' = \sqrt{R^2 - 2\rho a \cos(\varphi - \varphi')}$ and $R = \sqrt{(z - z')^2 + \rho^2 + a^2}$ and a is related to the inner and outer radii. This representation has been used in the analysis of radiation from cylindrical wires and loops.[68,69]

To study the THG in the proposed torus metasurface, we perform nonlinear optical simulations based on an undepleted pump approximation using COMSOL Multiphysics in the frequency domain.[70,71] In particular, a two-step simulation approach that exploits the undepleted pump approximation was used to obtain the harmonic generations that result from the proposed Si torus metasurface. The linear response of the torus structure was first simulated at fundamental frequencies. Next, the THG emission was acquired by using a linear electric field obtained from the first step as the source of the nonlinear polarization induced inside in the Si nanostructure. The elements of the nonlinear susceptibility tensor $\chi(3)$ are considered as constant scalar values of 2.45×10^{-19} $(\text{m V}^{-1})^2$. All THG responses were simulated based on a unit cell of the investigated structure by employing periodic boundary conditions. In Fig. 2(i–l), we illustrate the simulated THG spectra obtained by summing up the surface integrations of the THG signal on two virtual surfaces above and beneath the metasurface. Resonance-enhanced THG can be clearly seen. Normalized to the maximum THG intensity observed, the TD and MQ-X modes lead to THG significantly stronger than that seen at the MQ-M and MD modes. From the THG peak values, it can be seen that the MQ-X mode enables more than a 2 times (20 times) stronger THG compared with the ED + TD mode (MD mode), while the THG signal arising from the MQ-M mode is more than 3 orders lower. These observations reveal the different ways in which multipolar resonances can enhance THG in the proposed torus metasurface. It should be noted that the distinct mode profiles, especially the electric field distributions of the different multipolar resonances, determine their different behavior through nonlinear conversion. Moreover, nonlinear multipolar analysis can be employed to theoretically determine the mode-dependent contributions of each multipole to TH radiation.[71] We note that, despite these contribution differences, the intensity of the THG signal generated from the proposed torus metasurface is primarily determined by the value of the Q-factor, which determines the field enhancement effect, of each multipolar resonance. This is made evident from a comparison between the Q-factor analysis (Fig. 1c) and the THG spectra (Fig. 2(i–l)). Consequently, in our following discussions, we focus on the properties of the THG signals stemming from the TD and MQ-X modes. As the schematic in Fig. 2(m) shows, given the fact that the periodicity of the metasurface is larger than the wavelengths of the THG signals associated with the TD and MQ-X modes, the THG emitting from the metasurface can simultaneously couple to multiple diffraction channels.[72] Fig. 2(n) and (o) summarize the TD on-resonance THG intensity distributions between the diffraction orders in reflection and transmission, respectively. Note that the THG signal in reflection exists in

the (−1, 0), (1, 0), (0, −1), and (0, 1) diffraction orders, whereas, in transmission, THG also beams into the higher diffraction orders (±1, ±1) due to the refractive index of the glass substrate. Furthermore, the on-resonance THG intensity distributions related to the MD-X mode in the metasurface under a y-polarized excitation are shown in Fig. 2(p) and (q). We note that due to the anisotropy of the torus structure, THG ununiformly beams into different diffraction orders. For instance, in reflection (transmission) the TD THG signal in the order of (−1, 0) is ∼11% stronger (∼8% weaker) than that in the order of (1, 0), while the THG signal associated with MD-X mode in the order of (−1, 0) is ∼19% stronger (∼14% stronger) than that in the order of (1, 0). These observations indicate the flexibility offered by the torus metasurface in tailoring the diffraction efficiency of nonlinear generation. We note that, originating from optical anisotropy at the unit cell level, the control over diffraction efficiency observed under normal incidence in our study is distinct from the unevenly distributed THG diffractions recently observed in a Si bar array due to oblique excitations.[72] Furthermore, although the observed THG signals from the structure illustrated in Fig. 2(m) are near linearly polarized, the THG intensity control capability of the metasurface suggests the potential to exploit symmetry in torus resonators for manipulating the polarization of nonlinear generation. Moreover, considering the wavelengths of the THG signal emitted from the system and the periodicity of the structure, 2nd-order THG diffraction exists. Nevertheless, the strongest THG signal in the 2nd-order diffraction channels is about 5 times weaker than that in the 1st-order diffraction. Therefore, we focus here on the 1st-order THG signals and their properties. Lastly, the total THG conversion efficiency $\eta = P_{\text{THG}}/P_{\text{pump}}$ is about 3×10^{-3}, which is comparable to that previously observed in silicon metasurfaces that support quasi-BICs.[73]

Fig. 3(a) depicts a unit cell of a chiral torus metasurface having a broken in-plane mirror (2D-chiral) symmetry. The 2D-chiral symmetry is achieved by arranging the ten nanogrooves following $\sum_{i=1}^{10} \theta_i = 180°$ and $\Delta\theta = \theta_{i+1} - \theta_i$ which denotes the angular difference between every two neighboring nanogrooves (see the inset of Fig. 3(a)). Note that, $\Delta\theta = 0$ corresponds to an achiral structure, while $\Delta\theta > 0$ ($\Delta\theta < 0$) defines a right-handed (left-handed) chiral structure. In other words, the sign of $\Delta\theta$ determines the chiroptical characteristics of the torus metasurface, as seen in the later discussion. Fig. 3(b) illustrates the simulated circular polarization (CP) transmittance spectra when $\Delta\theta = 2°$ and the metasurface is illuminated by left- and right-handed circularly polarized (LCP and RCP) waves at normal incidence. T_{RR} (T_{LL}) and T_{RL} (T_{LR}) denote the co- and cross-polarization transmittance of an RCP (LCP) wave. Featured by the unequal CP transmittance, i.e., $T_{\text{RR}} \neq T_{\text{LL}}$ and $T_{\text{RL}} \neq T_{\text{LR}}$, two sharp chiral resonances (hereafter referred to as mode 1 and mode 2) are identified at wavelengths around 1101 nm and 1104.5 nm, respectively. Note that the $T_{\text{RR}} \neq T_{\text{LL}}$ characteristic arises from the C_1 rotational symmetry of the unit cell.[62] Fig. 3(c) depicts the corresponding transmission circular dichroism $T_{\text{CD}} = (T_{\text{RR}} + T_{\text{RL}}) - (T_{\text{LL}} + T_{\text{LR}})$, indicating
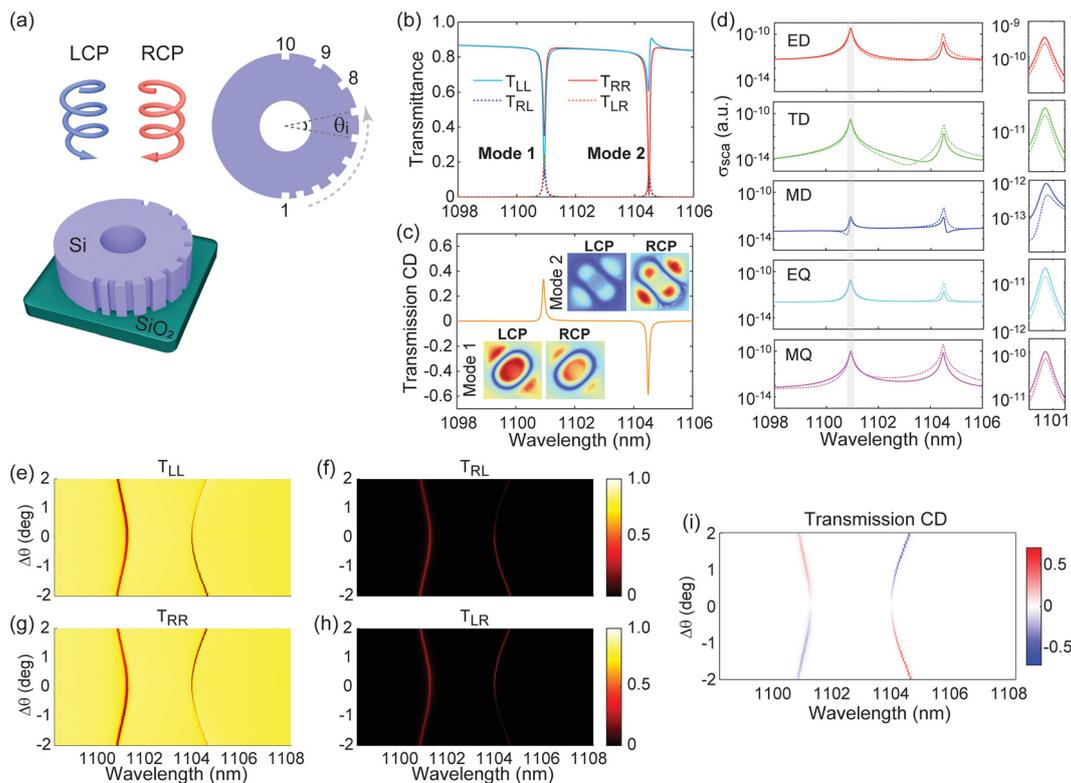
Fig. 3 Chiral torus metasurfaces. (a) Schematic of a unit cell. Insets: top-view of the structure showing the chiral arrangement of the nanogrooves determined by $\Delta\theta = \theta_{i+1} - \theta_i$. (b) Simulated CP transmittance spectra when $\Delta\theta = 2°$. (c) The corresponding transmission CD spectra. Insets: the magnitude of the electric field cut from the middle of the torus resonator under LCP and RCP excitation at mode 1 and mode 2. (d) Multipolar decomposition when the structure is illuminated by LCP (solid curves) and RCP (dashed curves) waves, respectively. A zoom-in spectrum corresponding to mode 1 (gray area) is shown on the right of each panel. CP transmittance spectra (e) T_{LL}, (f) T_{RL}, (g) T_{RR}, and (h) T_{LR} as a function of $\Delta\theta_i$. (i) The corresponding transmission CD spectra as a function of $\Delta\theta_i$.

the intrinsic handedness-selectivity of the chiral torus metasurface in the interaction with CP light at the two modes. This is made evident by the on-resonance electric field distributions, as shown in the insets of Fig. 3(c). In particular, the circular-polarization-dependent field concentration gives rise to not only the transmission CD in the linear regime but also the spin-selective THG as seen in later discussions. To further illustrate the origin of the observed chiral response, a multipolar decomposition analysis was conducted based on induced currents in the structure when it is illuminated by LCP and RCP waves, respectively. In Fig. 3(d) we compare the handedness-dependent excitations of multipolar modes (solid (dashed) curves correspond to an LCP (RCP) excitation). To better illustrate the comparison at mode 1 (the gray region), a zoom-in spectrum is shown on the right of each panel. It can be clearly seen that, at mode 1 (mode 2), all modes show larger scattering cross-section under an LCP (RCP) excitation. We note that two additional resonances were observed at wavelengths around 1230 nm and 1630 nm but exhibit negligible chiral response ($T_{CD} \approx 0$) (not shown). Regarding the MQ-M and MD resonances identified in Fig. 2(c) and (d), these two modes are insensitive to the chiral symmetry and will not be considered in our following discussion. We also note that

besides the asymmetric nanogroove arrangement, the other source of the observed chiroptical response is the difference between the refractive index of the glass substrate and the air on top of the metasurface.

To better illustrate the role of the 2D-chiral symmetry, Fig. 3 (e–h) depict the CP transmission of the metasurface as a function of $\Delta\theta$, while the corresponding transmission CD spectra are summarized in Fig. 3(i). When the value of $\Delta\theta$ changes sign (for instance from 2° to −2°), the metasurface exhibits a handedness-flipped chiroptical response upon interacting with CP waves, unambiguously demonstrating the enantiomeric characteristics of the corresponding torus meta-atoms. Furthermore, T_{CD} vanishes when $\Delta\theta$ approaches 0, featuring a chiral BIC with a Q-factor potentially going to infinity.[57–59] These results further reveal the potential utility of the proposed chiral torus metasurface for chiroptical response engineering. We note that chiroptical second harmonic generation (SHG) from plasmonic nanorods with local symmetry breaking has been reported recently,[74] suggesting that the symmetry property of optical resonators provides an additional knob that can be adjusted to control the polarization state of the generated harmonic signals. Therefore, the 2D-chiral symmetry is expected to enable chiral-resonance-mediated control over

polarization of THG signals emitted from the torus metasurfaces. It should be noted that here we primarily investigate the chirality arising from the nanogroove arrangement, while the chiroptical response, such as circular dichroism (CD), can be further improved through additional structural optimization involving other important geometrical parameters such as the thickness, inner/outer ring radius, *etc*. Furthermore, it has been demonstrated that arbitrary polarization manipulation can be achieved in single layer dielectric metasurfaces leveraging a combination of geometric phase with resonant and propagation phase.[75] The concept has been referred to as the hybrid phase modulation mechanism, which includes all degrees of freedom in the meta-atom design process, including the shape, size, rotational angle, *etc*.[76] In general, the polarization manipulation capability of a metasurface can be engineered through tailoring three properties of the resonators, *i.e.*, birefringence, eigen-polarization states, and retardance, as well as the incidence angle.[77] Here we have shown that varying the symmetry properties of the torus structure can facilitate strong interactions with linearly or circularly polarized incident waves. Nevertheless, in sharp contrast to the optical responses provided by the Mie-resonance-based unit cells (such as nano-cylinders[75]), the high-Q resonances associated with the quasi-BICs observed in our study may make it challenging to engineer the torus meta-atoms for arbitrary polarization manipulation.

To investigate the THG from the chiral torus metasurface ($\Delta\theta = 2°$), without loss of generality, we consider a scenario where the metasurface is excited by a linearly (x- or y-) polarized fundamental wave at normal incidence (Fig. 4(a)). T_{xx} (T_{yy})

and T_{yx} (T_{xy}) denote the co- and cross-polarization transmittance of an x-polarized (y-polarized) wave. Fig. 4(b) and (c) show the simulated transmittance spectra near mode 1 and mode 2, which, as a different form of results from that shown in Fig. 3(b), directly illustrate the response of the system under linearly polarized wave illumination. Fig. 4(d) and (e) (Fig. 4(f) and (g)) depict the THG spectra when the metasurface is excited by an x-polarized (y-polarized) wave in the same wavelength ranges. Similar to the results shown in Fig. 2(i–l), the THG spectra in Fig. 4 were obtained by collecting all THG signals emitting from the metasurface. The THG spectra were normalized to the peak THG intensity value when the metasurface is under x-polarized illumination at mode 1 (Fig. 4(c)). All THG spectra peak at the wavelengths where the chiral resonances match with the fundamental. Nevertheless, the peak values of the THG signals corresponding to x-polarized excitation (Fig. 4(d) and (e)) are significantly larger than those from y-polarized excitation (Fig. 4(f) and (g)). Consequently, in the following discussion we will focus on the x-pol-excitation on-resonance THG signals in both modes. Note that the handedness-dependent THG from the proposed chiral torus metasurface under circularly polarized excitation have also been investigated. The corresponding spectrum of the THG-CD = $(I_{\text{THG}}^{\text{RCP}} - I_{\text{THG}}^{\text{LCP}})/(I_{\text{THG}}^{\text{RCP}} + I_{\text{THG}}^{\text{LCP}})$, where $I_{\text{THG}}^{\text{RCP}}$ and $I_{\text{THG}}^{\text{LCP}}$ are the intensity of THG signals emitting from the metasuface under RCP and LCP excitations, respectively, indicates strong nonlinear circular dichroism at the wavelengths corresponding to the two chiral resonances in the linear regime (Fig. S2).

In Fig. 5, we summarize the diffraction and polarization properties of the on-resonance THG signals at mode 1 and mode 2.
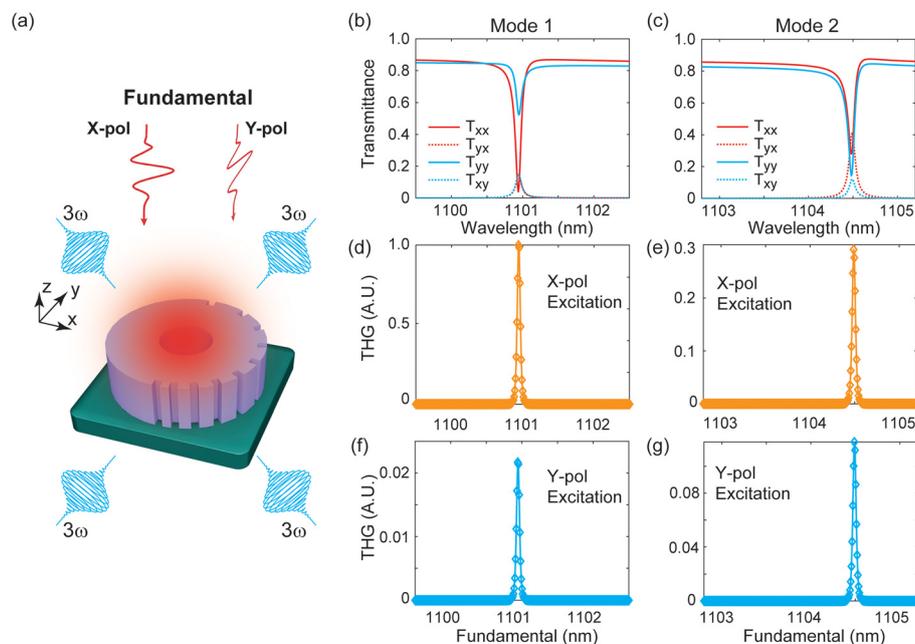

Fig. 4 THG in a chiral torus metasurface. (a) Schematic of the system under a linearly polarized excitation. Linear-polarization transmittance spectra at wavelengths around (b) mode 1 and (c) mode 2. THG spectra of the system under an x-polarized excitation at fundamental wavelengths around (d) mode 1 and (e) mode 2. (f and g) The same as panels (d and e), but for a y-polarized excitation.
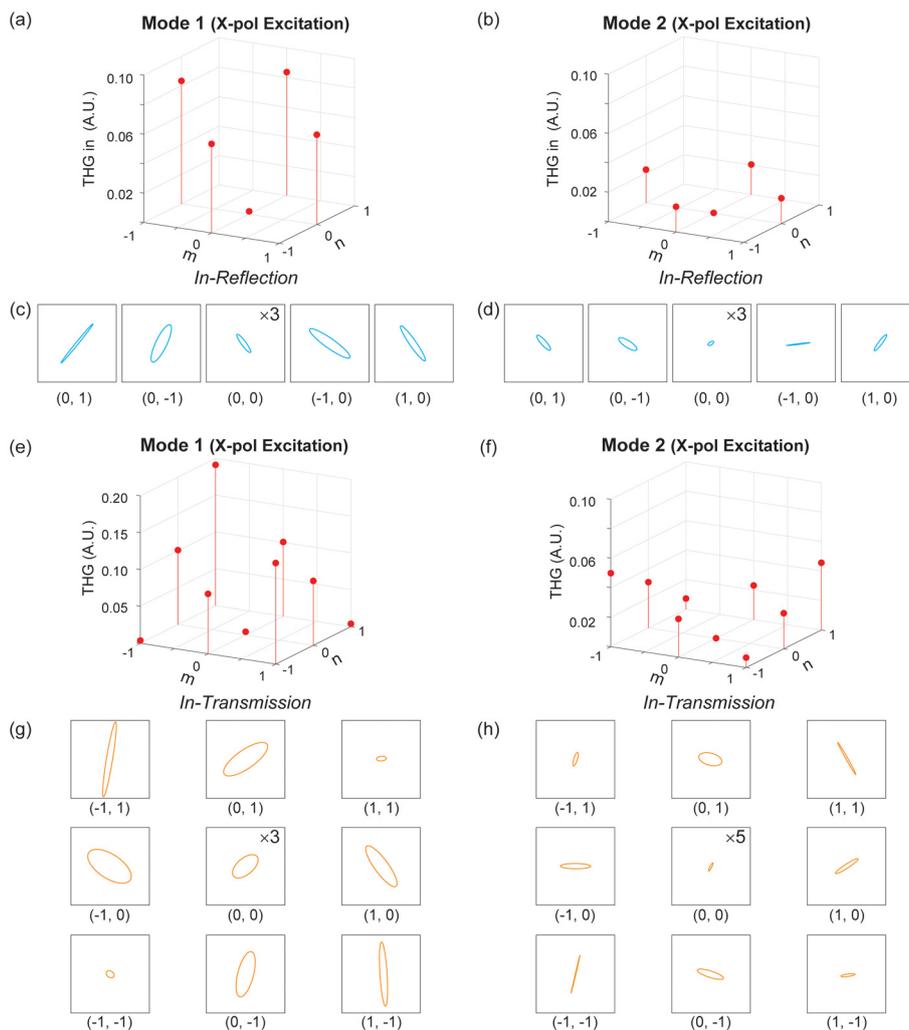
Fig. 5 Properties of on-resonance THG from the chiral torus metasurface. Power distribution between the diffraction orders in (a) mode 1 and (b) mode 2 in reflection. (c and d) The corresponding polarization ellipses. (e and f) The same as (a and b) panels, but in transmission. (g and h) The corresponding polarization ellipses.

Note that, for comparison purposes, the results corresponding to the THG signals in the direct reflection and transmission (*i.e.*, zero-order diffraction mode) are also presented. Fig. 5(a) and (b) depict the THG power distributions between the diffraction orders in reflection. At mode 1, THG intensity in the diffraction order of (−1, 0) is close to that in the order of (0, 1) but 38% stronger than those on the orders of (0, −1) and (1, 0). In contrast, at mode 2, THG intensity in the diffraction order of (−1, 0) is close to that in the (0, −1) order and is 29% stronger than those in the (0, 1) and (1, 0) orders. The unbalanced distributions between pairs of THG diffraction orders are more pronounced in transmission signals, as illustrated in Fig. 5(e) and (f). For instance, at mode 1, THG intensity in the diffraction order of (−1, 1) is 38% stronger than that in the (1, −1) order, while THG signals in the (−1, −1) and (1, 1) orders are almost completely suppressed. Moreover, at mode 2, THG intensity in the diffraction orders of (−1, −1) and (1, 1) is 6 times higher than those in the (1, −1) and (−1, 1) orders. This THG redistribution phenomenon can be

attributed to the asymmetric local electric field in the chiral torus at the two chiral modes, as illustrated in the insets of Fig. 3(c).[72] These observations clearly reveal the remarkable influence of the torus resonators' symmetry property on the THG distribution between diffraction channels.

On top of the diffraction redistribution effect, the chiral torus metasurface also exhibits the ability to control the polarization state of the emitting THG signals. Here, we define ellipticity as η = $\tan^{-1}[(|E_a| - |E_b|)/(|E_a| + |E_b|)]$, where $|E_a|$ and $|E_b|$ represent the semi-major and minor axes of the polarization ellipse of the electric field. We note that $\eta = 45°$ (0°) correspond to linearly (circularly) polarized waves. Fig. 5(c) and (d) illustrate the polarization ellipses of the THG signals generated from mode 1 coupled to diffraction channels in reflection (transmission). Hence, elliptically polarized THG is achieved. For TH emission in reflection (Fig. 5(c)), η achieves 29° and 32° in the diffraction orders of (0, −1) and (−1, 0), respectively. In transmission (Fig. 5(g)), among the channels of high THG efficiency, the

maximum $\eta = 19.5°$ is observed in the diffraction order of $(−1, 0)$, while elliptically polarized TH signals are also observed in orders of $(0, 1)$, $(1, 0)$, and $(0, −1)$. Interestingly, despite the low efficiency, THG signals in the $(0, 0)$ order, *i.e.*, direct reflection and transmission, are also elliptically polarized. Fig. 5(g) and (h) depict the polarization ellipses of the THG signals generated from mode 2, in which elliptically polarized THG are also seen. We note that the polarization states of the THG signals are simultaneously determined by all resonance modes seen from the multipolar decomposition. Further mode engineering can be implemented to improve, for instance, the circularity of emitted THG. These results further reveal the influence of the torus topology of the resonators on the intrinsic properties of nonlinear generation from the system.

3. Conclusion

To summarize, we have demonstrated that a silicon torus metasurface with a broken symmetry can support a series of resonances associated with bound states in the continuum. Moments including an electric dipole, a toroidal dipole, two magnetic quadrupoles, and a magnetic dipole are identified at near infrared wavelengths. Nanogrooves are introduced into the silicon torus to enable optical anisotropy, allowing polarization-sensitive excitations of the high-Q quasi-BIC ED, TD, MQ, and MD resonances. Nonlinear simulations show that those modes result in resonance-mediated enhanced third harmonic generation. Importantly, it is seen that the THG signal unevenly beams into different diffraction orders. This can be attributed to the asymmetric local electric field in the unit cells which is present at the resonances. Furthermore, by breaking the in-plane mirror symmetry, we identify two strong chiral resonances in a 2D-chiral metasurface that are associated with a TD mode and a MQ mode supported by the torus resonators, with a concomitant handedness-dependent field enhancement effect. Moreover, upon an on-resonance linearly polarized excitation, the chiral torus metasurface emits elliptically polarized THG signals, in which the corresponding THG efficiency between different diffraction orders is controlled by the symmetry of the local field in each unit cell. These observed properties reveal the potential of the torus metasurfaces for comprehensive manipulation of light in both the linear and nonlinear regimes.

Conflicts of interest

There are no conflicts to declare.

Data availability

The data that support the findings of this study are available from the corresponding author upon reasonable request.

Supplementary information (SI) is available. See DOI: https://doi.org/10.1039/d6nr00116e.

References

1 S. Eustis and M. A. El-Sayed, *Chem. Soc. Rev.*, 2006, **35**, 209.
2 I. Freestone, N. Meeks, M. Sax and C. Higgitt, *Gold Bull.*, 2007, **40**, 270.
3 W. Cai, U. K. Chettiar, H.-K. Yuan, V. C. de Silva, A. V. Kildishev, V. P. Drachev and V. M. Shalaev, *Opt. Express*, 2007, **15**, 3333.
4 J. Valentine, S. Zhang, T. Zentgraf, E. Ulin-Avila, D. A. Genov, G. Bartal and X. Zhang, *Nature*, 2008, **455**, 376.
5 J. K. Gansel, M. Thiel, M. S. Rill, M. Decker, K. Bade, V. Saile, G. von Freymann, S. Linden and M. Wegener, *Science*, 2009, **325**, 1513.
6 N. Yu, P. Genevet, M. A. Kats, F. Aieta, J.-P. Tetienne, F. Capasso and Z. Gaburro, *Science*, 2011, **334**, 333.
7 X. Yin, Z. Ye, J. Rho, Y. Wang and X. Zhang, *Science*, 2013, **339**, 1405.
8 V. V. Flambaum and I. B. Khriplovich, *Sov. Phys. JETP*, 1980, **52**, 5.
9 V. M. Dubovik and V. V. Tugushev, *Phys. Rep.*, 1990, **187**, 145.
10 V. V. Flambaum and D. W. Murray, *Phys. Rev. C*, 1997, **56**, 1641.
11 A. Ceulemans, L. F. Chibotaru and P. W. Fowler, *Phys. Rev. Lett.*, 1998, **80**, 1861.
12 I. B. Zel'Dovich, *Sov. Phys. JETP*, 1957, **33**, 1531.
13 V. M. Dubovik and A. A. Cheshkov, *Sov. J. Part. Nucl.*, 1975, **5**, 318.
14 G. N. Afanasiev, *J. Phys. A: Math. Gen.*, 1990, **23**, 5755.
15 G. N. Afanasiev and Y. P. Stepanovsky, *J. Phys. A: Math. Gen.*, 1995, **28**, 4565.
16 E. E. Radescu and D. H. Vlad, *Phys. Rev. E:Stat. Phys., Plasmas, Fluids, Relat. Interdiscip. Top.*, 1998, **57**, 6030.
17 E. E. Radescu and G. Vaman, *Phys. Rev. E:Stat., Nonlinear, Soft Matter Phys.*, 2002, **65**, 046609.
18 G. N. Afanasiev, *J. Phys. D: Appl. Phys.*, 2001, **34**, 539.
19 N. Papasimakis, V. A. Fedotov, K. Marinov and N. I. Zheludev, *Phys. Rev. Lett.*, 2009, **103**, 093901.
20 N. Papasimakis, V. A. Fedotov, V. Savinov, T. A. Raybould and N. I. Zheludev, *Nat. Mater.*, 2016, **15**, 263.
21 M. Gupta and R. Singh, *Rev. Phys.*, 2020, **5**, 100040.
22 M. Decker, S. Linden and M. Wegener, *Opt. Lett.*, 2009, **34**, 1579.
23 T. Kaelberer, V. A. Fedotov, N. Papasimakis, D. P. Tsai and N. I. Zheludev, *Science*, 2010, **330**, 1510.
24 M. Gupta and R. Singh, *Adv. Opt. Mater.*, 2016, **4**, 2119.
25 Z. Liu, S. Du, A. Cui, Z. Li, Y. Fan, S. Chen, W. Li, J. Li and C. Gu, *Adv. Mater.*, 2017, **29**, 1606298.

26 S. Wang, S. Wang, Q. Li, X. Zhao and J. Zhu, *Materials*, 2018, **11**, 2036.

27 V. A. Fedotov, A. V. Rogacheva, V. Savinov, D. P. Tsai and N. I. Zheludev, *Sci. Rep.*, 2013, **3**, 2967.

28 Z.-G. Dong, J. Zhu, J. Rho, J.-Q. Li, C. Lu, X. Yin and X. Zhang, *Appl. Phys. Lett.*, 2012, **101**, 144105.

29 M. Gupta, V. Savinov, N. Xu, L. Cong, G. Dayal, S. Wang, W. Zhang, N. I. Zheludev and R. Singh, *Adv. Mater.*, 2016, **28**, 8206.

30 A. A. Basharin, V. Chuguevsky, N. Volsky, M. Kafesaki and E. N. Economou, *Phys. Rev. B*, 2017, **95**, 035104.

31 A. E. Miroshnichenko, A. B. Evlyukhin, Y. F. Yu, R. M. Bakker, A. Chipouline, A. I. Kuznetsov, B. Luk'yanchuk, B. N. Chichkov and Y. S. Kivshar, *Nat. Commun.*, 2015, **6**, 8069.

32 J. S. Totero Gongora, A. E. Miroshnichenko, Y. S. Kivshar and A. Fratalocchi, *Nat. Commun.*, 2017, **8**, 15535.

33 L. Liu and L. Ge, *Opt. Express*, 2022, **30**, 7491.

34 R. Peng, Q. Zhao, Y. Meng and S. Wen, *Opt. Express*, 2022, **30**, 30799.

35 A. A. Basharin, M. Kafesaki, E. N. Economou, C. M. Soukoulis, V. A. Fedotov, V. Savinov and N. I. Zheludev, *Phys. Rev. X*, 2015, **5**, 011036.

36 S. Lepeshov and Y. Kivshar, *ACS Photonics*, 2018, **5**, 2888.

37 H. Duan, H. He, Y. Yi, L. Wang, Y. Zhang, S. You, Y. Wang, C. Gao, J. Huang and C. Zhou, *Opt. Lett.*, 2024, **49**, 5539.

38 Q. Zhao, J. Zhou, F. Zhang and D. Lippens, *Mater. Today*, 2009, **12**, 60.

39 S. Kruk and Y. Kivshar, *ACS Photonics*, 2017, **4**, 2638.

40 Y. Kivshar, *Natl. Sci. Rev.*, 2018, **5**, 144.

41 S. T. Ha, Y. H. Fu, N. K. Emani, Z. Pan, R. M. Bakker, R. Paniagua-Domínguez and A. I. Kuznetsov, *Nat. Nanotechnol.*, 2018, **13**, 1042.

42 K. Koshelev, S. Lepeshov, M. Liu, A. Bogdanov and Y. Kivshar, *Phys. Rev. Lett.*, 2018, **121**, 193903.

43 K. Koshelev, A. Bogdanov and Y. Kivshar, *Sci. Bull.*, 2019, **64**, 836.

44 K. Koshelev, Y. Tang, K. Li, D.-Y. Choi, G. Li and Y. Kivshar, *ACS Photonics*, 2019, **6**, 1639.

45 Z. Liu, Y. Xu, Y. Lin, J. Xiang, T. Feng, Q. Cao, J. Li, S. Lan and J. Liu, *Phys. Rev. Lett.*, 2019, **123**, 253901.

46 L. Kang, H. Bao and D. H. Werner, *Opt. Lett.*, 2021, **46**, 633.

47 Y. He, G. Guo, T. Feng, Y. Xu and A. E. Miroshnichenko, *Phys. Rev. B*, 2018, **98**, 161112.

48 S. You, L. Wang, H. He, C. Zhou and L. Huang, *Laser Photonics Rev.*, 2025, **19**, e00677.

49 Y. Zhao, M. A. Belkin and A. Alù, *Nat. Commun.*, 2012, **3**, 870.

50 Y. Cui, L. Kang, S. Lan, S. Rodrigues and W. Cai, *Nano Lett.*, 2014, **14**, 1021.

51 D. C. Hooper, A. G. Mark, C. Kuppe, J. T. Collins, P. Fischer and V. K. Valev, *Adv. Mater.*, 2017, **29**, 1605110.

52 J. T. Collins, D. C. Hooper, A. G. Mark, C. Kuppe and V. K. Valev, *ACS Nano*, 2018, **12**, 5445.

53 U. Kilic, M. Hilfiker, A. Ruder, R. Feder, E. Schubert, M. Schubert and C. Argyropoulos, *Adv. Funct. Mater.*, 2021, **31**, 2010329.

54 E. Plum and N. I. Zheludev, *Appl. Phys. Lett.*, 2015, **106**, 221901.

55 L. Kang, S. P. Rodrigues, M. Taghinejad, S. Lan, K.-T. Lee, Y. Liu, D. H. Werner, A. Urbas and W. Cai, *Nano Lett.*, 2017, **17**, 7102.

56 L. Kang, C.-Y. Wang, X. Guo, X. Ni, Z. Liu and D. H. Werner, *Nano Lett.*, 2020, **20**, 2047.

57 M. V. Gorkunov, A. A. Antonov and Y. S. Kivshar, *Phys. Rev. Lett.*, 2020, **125**, 093903.

58 A. Overvig, N. Yu and A. Alù, *Phys. Rev. Lett.*, 2021, **126**, 073001.

59 Y. Chen, H. Deng, X. Sha, W. Chen, R. Wang, Y.-H. Chen, D. Wu, J. Chu, Y. S. Kivshar, S. Xiao and C.-W. Qiu, *Nature*, 2023, **613**, 474.

60 T. Shi, Z.-L. Deng, G. Geng, X. Zeng, Y. Zeng, G. Hu, A. Overvig, J. Li, C.-W. Qiu, A. Alù, Y. S. Kivshar and X. Li, *Nat. Commun.*, 2022, **13**, 4111.

61 X. Zhang, Y. Liu, J. Han, Y. Kivshar and Q. Song, *Science*, 2022, **377**, 1215.

62 L. Kang, Y. Wu and D. H. Werner, *Adv. Opt. Mater.*, 2023, **11**, 2202658.

63 S. Kang, H. Li, J. Fan, J. Yu, B. Qu, P. Chen and X. Wu, *APL Mater.*, 2025, **13**, 011106.

64 M. Lawrence, D. R. Barton and J. A. Dionne, *Nano Lett.*, 2018, **18**, 1104.

65 B. Zhang, A. Dong, J. Wang, M. Qin, J. Liu, W. Huang, S. Xiao and H. Li, *Nano Lett.*, 2025, **25**, 4568.

66 J. Wang, H. Xu, J. Si, H. Wu, H. Wang, H. Qiu, H. Jiang, M. Qin, J.-Q. Liu, F. Wu and H. Li, *Appl. Phys. Lett.*, 2025, **127**, 061701.

67 A. Dong, Y. Zhu, H. Wu, J. Wang, M. Qin, J. Liu, F. Wu and H. Li, *Phys. Rev. B*, 2025, **111**, 075301.

68 R. Mittra and D. H. Werner, *Frontiers in Electromagnetics*, IEEE Press, New York, 2015.

69 M. F. Pantoja, J. Nagar, B. Lu and D. H. Werner, *ACS Photonics*, 2017, **4**, 509.

70 L. Carletti, S. S. Kruk, A. A. Bogdanov, C. De Angelis and Y. Kivshar, *Phys. Rev. Res.*, 2019, **1**, 023016.

71 L. Wang, S. Kruk, K. Koshelev, I. Kravchenko, B. Luther-Davies and Y. Kivshar, *Nano Lett.*, 2018, **18**, 3978.

72 K. I. Okhlopkov, A. Zilli, A. Tognazzi, D. Rocco, L. Fagiani, E. Mafakheri, M. Bollani, M. Finazzi, M. Celebrano, M. R. Shcherbakov, C. De Angelis and A. A. Fedyanin, *Nano Lett.*, 2021, **21**, 10438.

73 S. Xiao, M. Qin, J. Duan, F. Wu and T. Liu, *Phys. Rev. B*, 2022, **105**, 195440.

74 Z. Li, L. Kang, R. W. Lord, K. Park, A. Gillman, R. A. Vaia, R. E. Schaak, D. H. Werner and K. L. Knappenberger, *ACS Nanosci. Au*, 2022, **2**, 32.

75 A. Arbabi, Y. Horie, M. Bagheri and A. Faraon, *Nat. Nanotechnol.*, 2015, **10**, 937.

76 Y. Gao and Y. Ma, *Adv. Opt. Photonics*, 2025, **17**, 789.

77 Z. Shi, A. Y. Zhu, Z. Li, Y.-W. Huang, W. T. Chen, C.-W. Qiu and F. Capasso, *Sci. Adv.*, 2020, **6**, eaba3367.